

Enormous Fluid Antenna Systems (E-FAS)— Part II: Channel Estimation

Farshad Rostami Ghadi, *Member, IEEE*, Kai-Kit Wong, *Fellow, IEEE*,
Masoud Kaveh, *Member, IEEE*, Hao Xu, *Senior Member, IEEE*, Baiyang Liu, *Senior Member, IEEE*,
Kin-Fai Tong, *Fellow, IEEE*, and Chan-Byoung Chae, *Fellow, IEEE*

Abstract—Enormous fluid antenna systems (E-FAS) have recently emerged as a new wireless architecture in which intelligent metasurfaces act as guided electromagnetic interfaces, enabling surface-wave (SW) propagation with much lower attenuation and more control than conventional space-wave transmission. While prior work has reported substantial power gains under perfect channel state information (CSI), the impact of practical channel acquisition on E-FAS performance remains largely unexplored. This paper presents the first comprehensive analysis of E-FAS-assisted downlink transmission under pilot-based channel estimation. We develop an estimation framework for the equivalent end-to-end channel and derive closed-form expressions for the statistics of the minimum mean-square-error (MMSE) channel estimate and its estimation error. Building on these results, we analyze both single-user and multiuser operation while explicitly accounting for the training overhead. For the single-user case, we characterize the outage probability and achievable rate with imperfect CSI, and reveal an inherent signal-to-noise ratio (SNR) saturation phenomenon caused by residual self-interference. For the multiuser case, we study zero-forcing (ZF) precoding based on imperfect channel estimates and show that the system becomes interference-limited in the high SNR regime because of residual inter-user interference. Furthermore, we quantify the trade-off between spatial multiplexing gains and pilot overhead when the number of users increases. Analytical findings are validated via Monte Carlo simulations and benchmarked against least-squares (LS) estimation and conventional non-E-FAS transmission. The results reveal that despite CSI imperfections and training costs, E-FAS retains substantial performance advantages and provides robustness enabled by its amplified large-scale channel gain.

Index Terms—Enormous fluid antenna systems (E-FAS), channel state information (CSI), channel estimation, imperfect CSI, surface wave, zero-forcing (ZF), multiuser MIMO.

I. INTRODUCTION

A. Background

THE RAPIDLY-INCREASING demand for ultra-high data rates, enhanced reliability, and energy-efficient transmission has stimulated intensive research on new physical layer paradigms for next-generation wireless systems, a.k.a., sixth-generation (6G) [1], [2], [3]. To meet the demand, one push is to utilize high frequency bands but at high carrier frequencies, space wave transmission suffers from severe spherical spreading loss, limited diffraction capability, and strong sensitivity to blockage. These intrinsic propagation constraints fundamentally limit the communication performance in dense and non-line-of-sight (NLoS) environments [4], [5], [6].

In order to overcome these limitations, reconfigurable intelligent surfaces (RIS) have been introduced as programmable electromagnetic structures capable of manipulating incident waves through adjustable reflection and/or transmission coefficients [7], [8]. RIS-enabled systems reshape the propagation environment and provide additional beamforming gains. However, their operation remains governed by three-dimensional (3D) space wave propagation and typically incurs a double path-loss effect, while requiring accurate channel state information (CSI) over potentially large-scale surfaces [9].

Beyond manipulating the propagation environment through intelligent surfaces, a complementary research direction is the concept of fluid antenna systems (FAS) which focuses upon enhancing spatial adaptability at the transceiver side and has emerged as a new paradigm [10], [11]. More precisely, FAS is a system concept that treats the antenna as a reconfigurable physical-layer resource to broaden system design and network optimization [12], [13], [14], [15], [16]. Recent FAS prototypes have been reported adopting a variety of reconfigurable antenna technologies [17], [18], [19], [20], [21], [22], [23]. In [24], various implementations of FAS were compared.

FAS emphasizes on the antenna reconfigurability for shape and position flexibility for diversity and multiplexing benefits. Even on one single radio frequency (RF) chain, FAS can dynamically reconfigure its radiation position within a confined spatial region, effectively exploiting spatial diversity without increasing hardware complexity. This flexibility enables improved link reliability and diversity gains, particularly in small form factor devices. In recent years, a great deal of research has been conducted to examine the diversity gains enabled by antenna position reconfigurability [25], [26], [27], [28], [29],

The work of F. Rostami Ghadi and K. K. Wong is supported by the Engineering and Physical Sciences Research Council (EPSRC) under Grant EP/W026813/1. The work of H. Xu is supported by National Natural Science Foundation of China (NSFC) under Grants 62501152 and U25A20398, and the Fundamental Research Funds for the Central Universities under grant 2242025R10001. The work of B. Liu and K.-F. Tong is supported by Hong Kong Metropolitan University, Staff Research Start-Up Fund under Grant FRSF/2024/03. The work of C.-B. Chae is supported by the Institute for Information and Communication Technology Planning and Evaluation (IITP)/National Research Foundation of Korea (NRF) grant funded by the Ministry of Science and ICT (MSIT), South Korea, under Grant RS-2024-00428780 and 2022R1A5A1027646.

F. Rostami Ghadi and K. K. Wong are with the Department of Electronic and Electrical Engineering, University College London, London, United Kingdom. UK. K. K. Wong is also affiliated with the Department of Electronic Engineering, Kyung Hee University, Yongin-si, Gyeonggi-do 17104, Republic of Korea (e-mail: {f.rostamighadi, kai-kit.wong}@ucl.ac.uk).

M. Kaveh is with the Department of Information and Communication Engineering, Aalto University, Espoo, Finland (e-mail: masoud.kaveh@aalto.fi).

H. Xu is with the National Mobile Communications Research Laboratory, Southeast University, Nanjing 210096, China (e-mail: hao.xu@seu.edu.cn).

B. Liu and K. F. Tong are with the School of Science and Technology, Hong Kong Metropolitan University, Hong Kong SAR, China. B. Liu is also affiliated with School of Artificial Intelligence, Shenzhen Technology University, Shenzhen, China (e-mail: {byliu, ktong}@hkmu.edu.hk).

C.-B. Chae is with the School of Integrated Technology, Yonsei University, Seoul, 03722, Republic of Korea (e-mail: cbchae@yonsei.ac.kr).

Corresponding Author: Kai-Kit Wong.

[30]. Besides diversity, FAS also gives rise to a new class of index modulation schemes for capacity gain [31], [32], [33], [34]. Moreover, FAS has been combined with existing multiple access techniques for synergistic benefits [35], [36], [37]. In addition, FAS has been applied to improve integrated sensing and communication (ISAC) [38], [39], [40], [41], [42] and security performance [43], [44], [45], [46].

To enhance RIS-aided communication, [47], [48], [49], [50] considered the joint benefits of RIS and FAS-equipped users and illustrated extraordinary performance gains. Furthermore, the concept of FAS can be introduced into each element of RIS, resulting in the notion of fluid RIS (FRIS) where each element becomes a ‘fluid’ element capable of optimizing its radiation characteristics including phase of reflection, position of reflection and radiation pattern. This is motivated by the attempt to fully utilize the available space for diversity benefits without necessarily increasing the number of elements. FRIS design and analysis has been addressed in [51], [52], [53], [54], [55]. Recent studies have also extended it to fluid integrated reflecting and emitting surfaces (FIRES) [56], [57]

To summarize, although FAS is attractive, its normal use at the transceiver sides would not be able to reverse the drastic propagation loss in the high frequency bands (i.e., mmWave). Even with FRIS and more so RIS, the doubly fading and path-loss effects are still substantial and only limited performance at best is attained, let alone the associated complexity for CSI acquisition and the extensive joint optimization.

B. A New Communication Paradigm and Motivation

Recognizing that the propagation characteristics constrained by space-wave propagation mechanisms and 3D power spreading are the main problem, the spirit of position reconfigurability in FAS could indeed be useful, if it is applied in a much larger scale. This has led to the concept of enormous FAS (E-FAS) [58], [59], [60]. Specifically, an E-FAS is an ensemble of one or more coordinated intelligent surfaces (or engineered metasurfaces) that helps establish communication between the transmitter(s) and receiver(s). A distinctive feature is that the engineered metasurfaces can serve as guided electromagnetic interfaces instead of reflectors in conventional RISs. In particular, incident space waves are converted into surface waves (SWs) that propagate along quasi-two-dimensional structures with cylindrical spreading before being re-radiated towards intended users. This mechanism significantly reduces attenuation compared to spherical space-wave spreading and enables energy routing along walls, ceilings, and building facades. As a result, E-FAS provides substantial large-scale power saving while preserving simplicity in end-to-end optimization.

Despite the initial vision first proposed in 2021 [58], little is known regarding the performance of E-FAS and its design aspects. In [59], the electromagnetic modelling of E-FAS was discussed while [60] presented initial evidence of promising improvements in outage probability and ergodic rate. However, like most physical-layer techniques, CSI is crucial for E-FAS but this issue remains unexplored. In particular, the equivalent end-to-end channel comprises a slowly varying SW routing gain and a short-term fading component, while the underlying multi-segment propagation and hidden SW routing stages are

not directly observable at the base station (BS). These unique features fundamentally differentiate E-FAS from conventional space wave multiple-input multiple-output (MIMO) and call for an explicit investigation of pilot-based channel estimation and the resulting performance trade-offs under realistic CSI estimation techniques and training overhead.

C. Key Questions

As a consequence of the aforesaid two-timescale structure, the end-to-end channel must be inferred through pilot-based training over finite coherence intervals. Imperfect CSI is thus inevitable and fundamentally alters the system behavior. More importantly, imperfect CSI introduces two critical phenomena that are absent under perfect CSI: (i) residual self-interference, referring to the non-vanishing interference component induced by channel estimation errors due to beamforming mismatch, leading to signal-to-noise ratio (SNR) saturation at high transmit powers in single-user transmission, and (ii) residual multiuser interference under zero-forcing (ZF) precoding, resulting in the interference-limited regime at high SNR. Whether the substantial power gains by E-FAS persist under realistic CSI acquisition constraints therefore remains an open question.

The above observations motivate us for a systematic investigation of E-FAS-assisted transmission under imperfect CSI. In this regard, several fundamental questions arise:

- 1) How does pilot-based estimation affect the equivalent end-to-end channel statistics in E-FAS-assisted systems?
- 2) Also, does the SW-induced large-scale gain translate into proportional performance gains under imperfect CSI?
- 3) How do training overhead and spatial multiplexing interact in multiuser E-FAS-assisted systems?
- 4) Under what conditions does the system become noise-limited or interference-limited?

Answering the above is essential to understand the robustness of E-FAS and to quantify the trade-offs between SW gain, estimation accuracy, and spatial degrees of freedom (DoF).

D. Contributions

This paper provides the first comprehensive analytical study of E-FAS-assisted downlink transmission under imperfect CSI. The main contributions are summarized as follows:

- We develop a pilot-based channel estimation framework for the end-to-end channel and obtain closed-form expressions for the variances of the minimum mean-square-error (MMSE) estimate and the associated estimation error.
- For the single-user case, we derive analytical expressions for the outage probability and the achievable rate under imperfect CSI while explicitly accounting for the training overhead. We characterize the resulting SNR saturation behavior and quantify the loss relative to perfect CSI.
- For the multiuser downlink, we analyze ZF precoding based on imperfect channel estimates and obtain tractable expressions for the residual-interference-limited signal-to-interference-plus-noise ratio (SINR) and ergodic sum-rate. We reveal how the system transitions from noise-limited to interference-limited regimes at high SNR.
- Also, we investigate the interplay between pilot length, coherence interval, and the number of users, exposing the

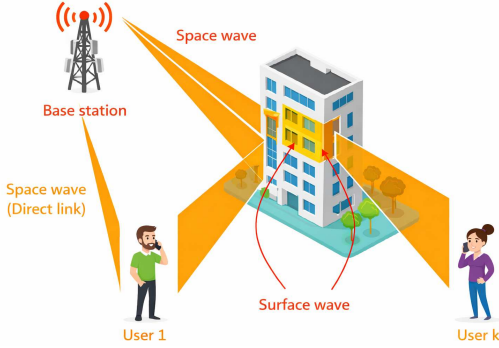


Fig. 1. Illustration of the E-FAS-assisted downlink system.

trade-off between spatial multiplexing gain and training overhead in E-FAS-assisted systems.

- Extensive Monte-Carlo simulations validate the accuracy of the derived analytical expressions and confirm the tight agreement between theory and simulation. MMSE and least squares (LS) estimators are benchmarked against the perfect CSI case and conventional non-E-FAS transmission. The results show that MMSE consistently outperforms LS, particularly at low pilot SNR and short training lengths, and that E-FAS maintains a pronounced SNR and sum-rate advantage over conventional transmission even under the practical situation where CSI is imperfect.

E. Organization and Notations

The remainder of this paper is organized as follows. Section II describes the system and channel models for E-FAS. Section III presents the pilot-based channel estimation framework and derives the statistics of the channel estimate channel and its error. Section IV analyzes the single-user case while Section V investigates multiuser ZF precoding with imperfect CSI estimates. Numerical results are provided in Section VI, and finally, we conclude this paper in Section VII.

Notations—Throughout this paper, scalars are denoted by italic letters, vectors by bold lowercase letters, and matrices by bold uppercase letters. The operators $(\cdot)^T$ and $(\cdot)^H$ denote the transpose and Hermitian transpose, respectively. The Euclidean norm of a vector is denoted by $\|\cdot\|$, and $|\cdot|$ represents the absolute value of a scalar. The expectation operator is denoted by $\mathbb{E}\{\cdot\}$. The notation $\mathcal{CN}(\mathbf{0}, \mathbf{R})$ denotes a circularly symmetric complex Gaussian distribution with zero mean and covariance matrix \mathbf{R} . The identity matrix of dimension M is denoted by \mathbf{I}_M . The Gamma function is denoted by $\Gamma(\cdot)$, and the lower incomplete Gamma function by $\Upsilon(\cdot, \cdot)$. Logarithms are taken with base 2 unless otherwise specified.

II. SYSTEM AND CHANNEL MODEL

A. System Architecture

As illustrated in Fig. 1, we consider the downlink of an E-FAS-assisted wireless network, in which an M -antenna BS simultaneously serves K single-antenna users. The propagation environment is instrumented with an E-FAS comprising distributed programmable metasurface tiles deployed on surrounding structures such as walls, ceilings, or building facades.

Unlike conventional reconfigurable metasurfaces that primarily reflect space waves, the E-FAS converts incident space waves into guided SWs, routes electromagnetic energy along engineered surface pathways, and re-radiates the signal toward intended users through programmable launcher structures.

For the model considered, we let $x_u \in \mathbb{C}$ denote the information symbol intended for user u , satisfying $\mathbb{E}\{|x_u|^2\} = 1$ and the BS applies linear precoding and transmits

$$\mathbf{x} = \sum_{u=1}^K \sqrt{P_u} \mathbf{w}_u x_u, \quad (1)$$

where $\mathbf{w}_u \in \mathbb{C}^M$ is the precoding vector associated with user u , P_u is the allocated transmit power, and $\sum_{u=1}^K P_u = P$ denotes the total BS transmit power. Therefore, the received signal at user u is then given by

$$y_u = \mathbf{h}_u^H \mathbf{x} + n_u, \quad (2)$$

where $\mathbf{h}_u \in \mathbb{C}^M$ represents the equivalent end-to-end BS-user channel induced by E-FAS-assisted propagation, and $n_u \sim \mathcal{CN}(0, \sigma^2)$ is additive white Gaussian noise (AWGN).

B. Physics-Informed Channel Representation

E-FAS propagation mechanism consists of multiple physical segments, including space wave transmission from the BS to the metasurface, guided SW propagation along programmable SW pathways, and re-radiation toward the users via launcher elements. A fundamental characteristic of this architecture is that the surface routing geometry and launcher configuration vary on a significantly slower timescale than the small-scale fading associated with the wireless segments. To capture this property, we adopt a two-timescale channel representation.

Specifically, the equivalent end-to-end channel of user u can be conveniently modeled as

$$\mathbf{h}_u = \sqrt{\beta_u} \mathbf{g}_u, \quad (3)$$

where $\beta_u > 0$ denotes the large-scale E-FAS routing gain and $\mathbf{g}_u \in \mathbb{C}^M$ represents the small-scale fading component. The parameter β_u captures the cumulative effect of SW attenuation along routed paths, junction losses, launcher efficiency, and routing geometry, while \mathbf{g}_u models the stochastic short-term fading arising from the wireless segments before and after SW propagation. Under physically consistent modeling of the wireless segments before and after SW propagation, the equivalent small-scale fading component follows an independent and identically distributed (i.i.d.) Rayleigh distribution across the BS antennas, i.e., $\mathbf{g}_u \sim \mathcal{CN}(\mathbf{0}, \mathbf{I}_M)$, as established in [59], [60]. Meanwhile, the large-scale routing gain β_u is determined by the E-FAS topology and evolves on a distinct slow routing timescale. Accordingly, the equivalent channel follows

$$\mathbf{h}_u \sim \mathcal{CN}(\mathbf{0}, \beta_u \mathbf{I}_M). \quad (4)$$

Moreover, the large-scale routing gain β_u evolves on a slow routing timescale T_r , determined by E-FAS configuration and environmental geometry, whereas the small-scale fading component \mathbf{g}_u varies over the conventional channel coherence time T_c , with $T_r \gg T_c$. This separation between routing-induced large-scale effects and small-scale fading constitutes a distinctive feature of E-FAS-assisted channels.

C. Signal Model

Substituting the equivalent channel model into the received signal expression yields

$$y_u = \sqrt{\beta_u} \mathbf{g}_u^H \mathbf{x} + n_u. \quad (5)$$

In the single-user case, i.e., $K = 1$, the received signal is simplified to

$$y = \sqrt{P\beta} \mathbf{g}^H \mathbf{w}x + n, \quad (6)$$

where \mathbf{w} is a unit-norm precoding vector.

In the multiuser case, i.e., $K \geq 1$, substituting the transmit signal into the received signal expression yields

$$y_u = \sqrt{P_u \beta_u} \mathbf{g}_u^H \mathbf{w}_u x_u + \sum_{i \neq u} \sqrt{P_i \beta_i} \mathbf{g}_u^H \mathbf{w}_i x_i + n_u, \quad (7)$$

where the first term corresponds to the desired signal component and the second term represents inter-user interference.

Note that the BS does not observe the individual physical segments, e.g., SW routing or launcher parameters, separately. Instead, it acquires only the composite channel vector \mathbf{h}_u . Furthermore, due to the two-timescale nature of E-FAS-assisted propagation, the large-scale routing gain β_u and the small-scale fading component \mathbf{g}_u may require different estimation strategies, which will be developed next.

III. TWO-TIMESCALE CHANNEL ESTIMATION FRAMEWORK

In this section, we develop a channel estimation framework tailored to the intrinsic two-timescale structure of E-FAS-assisted propagation introduced in Section II. In particular, the equivalent end-to-end channel comprises a slowly varying topology-dependent routing gain and a fast small-scale fading component. This separation naturally motivates a decoupled estimation procedure: (i) the routing gain is learned over a slow timescale via long-term pilot energy averaging, while (ii) the fast fading component is estimated per coherence block using MMSE principles. Unlike conventional MIMO settings where large-scale fading is purely geometry-induced and not reconfigurable, in E-FAS, the routing gain depends on the SW topology and directly affects the pilot observation quality, thereby coupling channel acquisition with routing design.

A. Training Protocol

Consider a time-division duplex (TDD) system and exploit channel reciprocity for downlink channel acquisition via uplink pilot transmission. During each coherence block of length T_c , the users transmit pilot sequences of length τ_p symbols. Let ρ_p denote the pilot transmit power per symbol. Each user u is assigned an orthogonal pilot sequence $\phi_u \in \mathbb{C}^{\tau_p}$ of length τ_p , satisfying $\phi_u^H \phi_i = 0$ for $u \neq i$ and $\|\phi_u\|^2 = \tau_p$. During the uplink training phase, the BS correlates the received pilot signal with ϕ_u to isolate the contribution of user u . Then the resulting sufficient statistic is given by [61]

$$\mathbf{y}_{p,u} = \sqrt{\tau_p \rho_p} \mathbf{h}_u + \mathbf{n}_{p,u}, \quad (8)$$

where $\mathbf{n}_{p,u} \sim \mathcal{CN}(\mathbf{0}, \sigma^2 \mathbf{I}_M)$ is AWGN after despreading.

Now, recalling from (3), the observation becomes

$$\mathbf{y}_{p,u} = \sqrt{\tau_p \rho_p \beta_u} \mathbf{g}_u + \mathbf{n}_{p,u}. \quad (9)$$

Importantly, the BS observes only the composite end-to-end channel realization and does not have direct access to the routing gain β_u or the individual physical propagation segments. Nevertheless, under physically consistent modeling of the multi-segment propagation, the equivalent channel admits a tractable Gaussian representation in which the topology-dependent routing gain appears as a distinct large-scale parameter evolving on a slow timescale. This structure preserves analytical tractability while explicitly coupling channel acquisition with routing configuration.

B. Estimation of the Short-Term Fading Component

Since the slow routing gain β_u evolves on a much larger timescale than the coherence block, it can be treated as quasi-static during fast fading estimation. Conditioned on this slowly varying routing parameter, the estimation problem reduces to recovering the small-scale fading vector \mathbf{g}_u from the sufficient statistic $\mathbf{y}_{p,u}$. Although the resulting estimator follows standard MMSE principles for Gaussian channels, its performance is directly governed by the topology-dependent routing gain β_u , which determines the effective pilot observation quality. This coupling between routing configuration and estimation accuracy is intrinsic to E-FAS-assisted propagation.

By exploiting the joint Gaussian structure of \mathbf{g}_u and $\mathbf{y}_{p,u}$, the linear MMSE estimator is obtained in closed form as

$$\hat{\mathbf{g}}_u = \frac{\sqrt{\tau_p \rho_p \beta_u}}{\tau_p \rho_p \beta_u + \sigma^2} \mathbf{y}_{p,u}. \quad (10)$$

Therefore, the estimation error is defined as

$$\tilde{\mathbf{g}}_u = \mathbf{g}_u - \hat{\mathbf{g}}_u, \quad (11)$$

where $\hat{\mathbf{g}}_u$ and $\tilde{\mathbf{g}}_u$ are statistically independent under Gaussian assumptions and their covariance matrices are given by

$$\mathbb{E}\{\hat{\mathbf{g}}_u \hat{\mathbf{g}}_u^H\} = \frac{\tau_p \rho_p \beta_u}{\tau_p \rho_p \beta_u + \sigma^2} \mathbf{I}_M \quad (12)$$

and

$$\mathbb{E}\{\tilde{\mathbf{g}}_u \tilde{\mathbf{g}}_u^H\} = \frac{\sigma^2}{\tau_p \rho_p \beta_u + \sigma^2} \mathbf{I}_M. \quad (13)$$

Thus, the equivalent channel estimate is reconstructed as

$$\hat{\mathbf{h}}_u = \sqrt{\beta_u} \hat{\mathbf{g}}_u, \quad (14)$$

which yields the orthogonal decomposition

$$\mathbf{h}_u = \hat{\mathbf{h}}_u + \tilde{\mathbf{h}}_u, \quad (15)$$

where $\tilde{\mathbf{h}}_u = \sqrt{\beta_u} \tilde{\mathbf{g}}_u$. Consequently, the scalar estimation variances are therefore given by

$$\Omega_{\hat{h},u} = \frac{\tau_p \rho_p \beta_u^2}{\tau_p \rho_p \beta_u + \sigma^2} \quad (16)$$

and

$$\Omega_{\tilde{h},u} = \beta_u - \Omega_{\hat{h},u}. \quad (17)$$

These expressions reveal that the estimation accuracy improves with increasing pilot energy $\tau_p \rho_p$ and routing gain β_u . Specifically, stronger routing enhances the pilot observation quality and reduces the estimation error variance, improving the reliability of subsequent precoding operations.

C. Slow-Timescale Estimation of the Routing Gain

The routing gain β_u varies on a much slower timescale $T_r \gg T_c$, since it is determined by the large-scale SW routing geometry rather than the small-scale fading. Therefore, β_u can be estimated using long-term averaging of the received pilot energy across multiple coherence blocks.

Let B denote the number of coherence blocks used for averaging, and let $\mathbf{y}_{p,u}^{(b)}$ denote the pilot observation in block b . From the pilot model, we have

$$\mathbf{y}_{p,u}^{(b)} = \sqrt{\tau_p \rho_p \beta_u} \mathbf{g}_u^{(b)} + \mathbf{n}_{p,u}^{(b)}. \quad (18)$$

Under the i.i.d. Rayleigh fading channel assumption, i.e., $\mathbf{g}_u \sim \mathcal{CN}(\mathbf{0}, \mathbf{I}_M)$, we have

$$\mathbb{E}\{\|\mathbf{g}_u\|^2\} = M. \quad (19)$$

Hence, the average received pilot energy satisfies

$$\mathbb{E}\{\|\mathbf{y}_{p,u}\|^2\} = \tau_p \rho_p \beta_u M + M \sigma^2. \quad (20)$$

An unbiased estimator of β_u can thus be constructed as

$$\hat{\beta}_u = \frac{1}{B \tau_p \rho_p M} \sum_{b=1}^B \|\mathbf{y}_{p,u}^{(b)}\|^2 - \frac{\sigma^2}{\tau_p \rho_p}. \quad (21)$$

By the law of large numbers, $\hat{\beta}_u$ converges almost surely to β_u as $B \rightarrow \infty$. This two-timescale separation enables infrequent estimation of the routing gain, while short-term fading estimation is performed per coherence block, thereby reducing training overhead and improving scalability.

The above framework reveals a distinctive property of E-FAS-assisted systems: channel estimation quality depends not only on pilot resources (τ_p, ρ_p) but also on the routing gain β_u . Stronger SW routing increases the effective pilot observation SNR, thereby improving CSI accuracy in addition to enhancing the received signal power. Since β_u evolves on a slow timescale, the proposed two-timescale structure reduces the need for frequent large-scale parameter learning.

D. Impact of Finite Averaging on Routing Gain Estimation

The convergence result above holds asymptotically as $B \rightarrow \infty$. In practice, nevertheless, the routing gain β_u is estimated over a finite number of coherence blocks, and therefore $\hat{\beta}_u$ is subject to estimation uncertainty.

While β_u was assumed known to derive the MMSE estimator in closed form, in practice the BS employs the slow-timescale estimate $\hat{\beta}_u$ obtained in (21). It is important to emphasize that the uncertainty considered here stems from finite-sample pilot averaging rather than from large-scale shadowing randomness. Accordingly, in order to capture the impact of finite averaging in a tractable manner, we adopt a first-order multiplicative approximation

$$\hat{\beta}_u = \beta_u (1 + \epsilon_u), \quad (22)$$

where ϵ_u is a zero-mean random variable with variance $\sigma_{\epsilon,u}^2$, operating in the practically relevant regime where $\sigma_{\epsilon,u}^2 \ll 1$. An equivalent additive representation $\hat{\beta}_u = \beta_u + \delta_u$ may also be adopted, where $\delta_u = \beta_u \epsilon_u$ and $\mathbb{E}\{|\delta_u|^2\} = \beta_u^2 \sigma_{\epsilon,u}^2$. Since $\hat{\beta}_u$ is constructed by averaging B independent pilot-energy realizations, its variance decreases with the averaging window size. Therefore, under the i.i.d. Rayleigh assumption and finite second-order moments of $\|\mathbf{y}_{p,u}\|^2$, the estimation error variance scales approximately as

$$\sigma_{\epsilon,u}^2 \propto \frac{1}{B}. \quad (23)$$

Therefore, increasing the slow-timescale averaging window B improves the accuracy of the routing gain estimate without affecting the fast-timescale pilot overhead.

When $\hat{\beta}_u$ is used in place of β_u for fast fading estimation, the MMSE estimator and the resulting channel estimate are computed using $\hat{\beta}_u$. Consequently, the scalar estimation variances $\Omega_{\hat{h},u}$ and $\Omega_{\tilde{h},u}$ become random quantities obtained by replacing β_u with $\hat{\beta}_u$ in their definitions. This induces additional variability in the residual self-interference and multiuser interference terms (to be analyzed in the following sections). Nevertheless, since $\sigma_{\epsilon,u}^2$ decreases with B , the impact of routing gain uncertainty can be made arbitrarily small by moderate slow-timescale averaging, thereby preserving the main performance advantages of E-FAS-assisted transmission. All subsequent performance analyses condition on the routing gain estimate $\hat{\beta}_u$, while the mismatch impact vanishes asymptotically as the averaging window size B increases.

Remark 1 (Mismatched MMSE Estimation). *When the slow-timescale estimate $\hat{\beta}_u$ replaces the true routing gain β_u in the MMSE estimator, the resulting fast-fading estimator becomes mismatched [62], [63]. Consequently, the estimation variances in (16) and (17) are exact only when β_u is perfectly known. However, since the variance of the routing gain estimation error satisfies $\sigma_{\epsilon,u}^2 \propto 1/B$, the mismatch effect diminishes as the averaging window size B increases. For sufficiently large B , the analytical expressions derived under perfect routing gain knowledge remain highly accurate.*

Remark 2. *To ensure that routing gain uncertainty has negligible impact on the high-SNR saturation level, the averaging window B may be selected such that $\sigma_{\epsilon,u}^2 \leq \sigma_{\epsilon,\max}^2$ for a target tolerance. Since $\sigma_{\epsilon,u}^2 \propto 1/B$, the required B grows linearly with $1/\sigma_{\epsilon,\max}^2$.*

IV. SINGLE-USER PERFORMANCE UNDER IMPERFECT CSI

Here, we analyze the performance of an E-FAS-assisted system in the single-user case. The analysis explicitly accounts for the two-timescale channel structure and the MMSE estimation framework developed in Section III.

A. Transmission Model

Consider the single-user case and omit the user index for notational clarity. The channel admits the decomposition

$$\mathbf{h} = \hat{\mathbf{h}} + \tilde{\mathbf{h}}, \quad (24)$$

where $\hat{\mathbf{h}}$ and $\tilde{\mathbf{h}}$ denote the MMSE estimate and the corresponding estimation error, respectively, which are statistically independent. Besides, the BS employs maximum ratio transmission (MRT) based on the estimated channel such that

$$\mathbf{w} = \frac{\hat{\mathbf{h}}}{\|\hat{\mathbf{h}}\|}. \quad (25)$$

Therefore, the transmitted signal is $\mathbf{x} = \sqrt{P}\mathbf{w}x$ in which $\mathbb{E}\{|x|^2\} = 1$. Hence, the received signal is given by

$$y = \sqrt{P}\mathbf{h}^H\mathbf{w}x + n, \quad (26)$$

where $n \sim \mathcal{CN}(0, \sigma^2)$.

B. Instantaneous SINR

Substituting the channel decomposition of (24) yields

$$y = \sqrt{P}\hat{\mathbf{h}}^H\mathbf{w}x + \sqrt{P}\tilde{\mathbf{h}}^H\mathbf{w}x + n. \quad (27)$$

Treating the unknown error term as additional Gaussian noise and conditioning on the channel estimate, the instantaneous SINR can be expressed as

$$\gamma = \frac{P|\hat{\mathbf{h}}^H\mathbf{w}|^2}{P\mathbb{E}\{|\tilde{\mathbf{h}}^H\mathbf{w}|^2 | \hat{\mathbf{h}}\} + \sigma^2}. \quad (28)$$

Since \mathbf{w} is a deterministic function of $\hat{\mathbf{h}}$ and $\tilde{\mathbf{h}}$ is independent of $\hat{\mathbf{h}}$, the interference term becomes

$$\mathbb{E}\{|\tilde{\mathbf{h}}^H\mathbf{w}|^2 | \hat{\mathbf{h}}\} = \mathbf{w}^H \mathbf{C}_{\tilde{\mathbf{h}}}\mathbf{w}, \quad (29)$$

where $\mathbf{C}_{\tilde{\mathbf{h}}} = \mathbb{E}\{\tilde{\mathbf{h}}\tilde{\mathbf{h}}^H\}$ denotes the error covariance matrix.

Under the uncorrelated Rayleigh fading assumption, i.e., $\mathbf{C}_{\tilde{\mathbf{h}}} = \Omega_{\tilde{\mathbf{h}}}\mathbf{I}_M$, and we therefore have

$$\mathbb{E}\{|\tilde{\mathbf{h}}^H\mathbf{w}|^2\} = \Omega_{\tilde{\mathbf{h}}}. \quad (30)$$

Moreover, MRT yields

$$|\hat{\mathbf{h}}^H\mathbf{w}|^2 = \|\hat{\mathbf{h}}\|^2. \quad (31)$$

Hence, the instantaneous SINR simplifies to

$$\gamma = \frac{P\|\hat{\mathbf{h}}\|^2}{P\Omega_{\tilde{\mathbf{h}}} + \sigma^2}. \quad (32)$$

C. Distribution of the Effective Channel Gain

Under the two-timescale model, the estimated equivalent channel is expressed as

$$\hat{\mathbf{h}} = \sqrt{\beta}\hat{\mathbf{g}}. \quad (33)$$

As a result, the MMSE estimate satisfies

$$\hat{\mathbf{h}} \sim \mathcal{CN}(\mathbf{0}, \Omega_{\hat{\mathbf{h}}}\mathbf{I}_M), \quad (34)$$

where

$$\Omega_{\hat{\mathbf{h}}} = \frac{\tau_p \rho_p \beta^2}{\tau_p \rho_p \beta + \sigma^2}. \quad (35)$$

Therefore, the entries of $\hat{\mathbf{h}}$ are i.i.d. complex Gaussian random variables with variance $\Omega_{\hat{\mathbf{h}}}$. Consequently, the squared norm

$$\|\hat{\mathbf{h}}\|^2 = \sum_{m=1}^M |\hat{h}_m|^2 \quad (36)$$

is the sum of M independent exponential random variables with mean $\Omega_{\hat{\mathbf{h}}}$. Hence, $\|\hat{\mathbf{h}}\|^2$ follows a Gamma distribution with shape parameter M and scale parameter $\Omega_{\hat{\mathbf{h}}}$ [64], i.e.,

$$\|\hat{\mathbf{h}}\|^2 \sim \Gamma(M, \Omega_{\hat{\mathbf{h}}}). \quad (37)$$

Now, by letting $Z \triangleq \|\hat{\mathbf{h}}\|^2$, the corresponding probability density function (PDF) is given by

$$f_Z(z) = \frac{z^{M-1}}{\Gamma(M)\Omega_{\hat{\mathbf{h}}}^M} \exp\left(-\frac{z}{\Omega_{\hat{\mathbf{h}}}}\right), \quad z \geq 0, \quad (38)$$

where $\Gamma(\cdot)$ denotes the Gamma function.

D. Outage Probability

For a target spectral efficiency R_{th} (in bps/Hz), an outage event is defined as

$$P_{\text{out}} \triangleq \Pr\left(\left(1 - \frac{\tau_p}{T_c}\right) \log_2(1 + \gamma) < R_{\text{th}}\right), \quad (39)$$

where $(1 - \tau_p/T_c)$ accounts for the pilot overhead within each coherence block. Equivalently, the outage condition can be expressed in terms of an SINR threshold $\gamma_{\text{th}} = 2^{\frac{R_{\text{th}}}{1 - \tau_p/T_c}} - 1$, such that $P_{\text{out}} = \Pr(\gamma < \gamma_{\text{th}})$. Using the SINR expression in (32), the outage probability can be rewritten as

$$P_{\text{out}} = \Pr\left(\|\hat{\mathbf{h}}\|^2 < \frac{(P\Omega_{\tilde{\mathbf{h}}} + \sigma^2)\gamma_{\text{th}}}{P}\right). \quad (40)$$

Since $\|\hat{\mathbf{h}}\|^2 \sim \Gamma(M, \Omega_{\hat{\mathbf{h}}})$, the outage probability corresponds to the cumulative distribution function (CDF) of a Gamma random variable evaluated at $x_{\text{th}} \triangleq \frac{(P\Omega_{\tilde{\mathbf{h}}} + \sigma^2)\gamma_{\text{th}}}{P}$. Therefore, it has the closed-form expression given by

$$P_{\text{out}} = \frac{\Upsilon\left(M, \frac{(P\Omega_{\tilde{\mathbf{h}}} + \sigma^2)\gamma_{\text{th}}}{P}\right)}{\Gamma(M)}, \quad (41)$$

where $\Upsilon(\cdot, \cdot)$ denotes the lower incomplete Gamma function.

E. Achievable Rate with Training Overhead

Due to pilot transmission, only a fraction of each coherence block is available for data transmission. Accounting for this training overhead, the achievable ergodic rate is given by

$$R = \left(1 - \frac{\tau_p}{T_c}\right) \mathbb{E}\{\log_2(1 + \gamma)\}, \quad (42)$$

where τ_p is the pilot length. Substituting the SINR expression from (32) into (42), the ergodic rate becomes

$$R = \left(1 - \frac{\tau_p}{T_c}\right) \mathbb{E}\left[\log_2\left(1 + \frac{P\|\hat{\mathbf{h}}\|^2}{P\Omega_{\tilde{\mathbf{h}}} + \sigma^2}\right)\right]. \quad (43)$$

Since $\|\hat{\mathbf{h}}\|^2 \sim \Gamma(M, \Omega_{\hat{\mathbf{h}}})$, the expectation can be found as

$$R = \frac{1 - \frac{\tau_p}{T_c}}{\ln 2} \times \int_0^\infty \ln\left(1 + \frac{Px}{P\Omega_{\tilde{\mathbf{h}}} + \sigma^2}\right) \frac{x^{M-1}}{\Gamma(M)\Omega_{\hat{\mathbf{h}}}^M} \exp\left(-\frac{x}{\Omega_{\hat{\mathbf{h}}}}\right) dx \quad (44)$$

$$= \left(1 - \frac{\tau_p}{T_c}\right) \frac{e^z}{\ln 2} \sum_{k=1}^M \text{E}_k(z), \quad (45)$$

where $z = \frac{P\Omega_{\hat{h}} + \sigma^2}{P\Omega_{\tilde{h}}}$ and $E_n(z) \triangleq \int_1^\infty \frac{e^{-zt}}{t^n} dt$ for $z > 0$ is the generalized exponential integral of order n . The proof of (45) is given in Appendix A.

F. High-SNR Behavior

As $P \rightarrow \infty$, the instantaneous SINR in (32) converges to

$$\gamma_\infty = \frac{\|\hat{\mathbf{h}}\|^2}{\Omega_{\tilde{h}}}. \quad (46)$$

Unlike the perfect CSI case, where γ grows unboundedly with P , the imperfect CSI system exhibits SINR saturation due to the residual self-interference term that scales linearly with P . Accordingly, the achievable rate converges to the finite limit

$$R_\infty = \left(1 - \frac{\tau_p}{T_c}\right) \mathbb{E} \left[\log_2 \left(1 + \frac{\|\hat{\mathbf{h}}\|^2}{\Omega_{\tilde{h}}}\right) \right]. \quad (47)$$

Importantly, the estimation variances $\Omega_{\hat{h}}$ and $\Omega_{\tilde{h}}$ depend explicitly on the routing gain β . A larger β improves the effective pilot SNR, thereby reducing $\Omega_{\tilde{h}}$ and increasing the saturation level. Hence, SW-assisted propagation improves not only the received signal strength but also the robustness of CSI acquisition. This intrinsic coupling between propagation geometry and estimation accuracy highlights a distinctive feature of E-FAS-assisted systems, where the topology-dependent routing gain directly governs both received signal strength and CSI quality. In contrast to conventional space wave MIMO systems with fixed large-scale fading, the routing configuration in E-FAS influences the effective pilot observation SNR and thus the estimation-induced interference level.

V. MULTIUSER TRANSMISSION UNDER IMPERFECT CSI

Consider the downlink transmission to K single-antenna users served by an M -antenna BS, where $K < M$. The analysis explicitly accounts for the two-timescale structure and the MMSE estimation framework developed in Section III.

A. ZF Precoding Based on Channel Estimates

Let $\hat{\mathbf{H}} = [\hat{\mathbf{h}}_1, \dots, \hat{\mathbf{h}}_K] \in \mathbb{C}^{M \times K}$ represent the estimated channel matrix. Provided that $M > K$, the BS constructs the ZF precoder as [62]

$$\mathbf{W} = \hat{\mathbf{H}} \left(\hat{\mathbf{H}}^H \hat{\mathbf{H}} \right)^{-1} \mathbf{D}, \quad (48)$$

where the diagonal matrix $\mathbf{D} = \text{diag}\{d_1, \dots, d_K\}$ is chosen such that $\|\mathbf{w}_u\|^2 = 1$ for all u , ensuring that

$$\mathbb{E}\{\|\mathbf{x}\|^2\} = \sum_{u=1}^K P_u = P. \quad (49)$$

We also define \mathbf{w}_u as the u -th column of \mathbf{W} . Hence, the transmitted signal is given by

$$\mathbf{x} = \sum_{u=1}^K \sqrt{P_u} \mathbf{w}_u x_u, \quad (50)$$

where $\mathbb{E}\{|x_u|^2\} = 1$.

B. Received Signal Model

The true channel admits the decomposition

$$\mathbf{h}_u = \hat{\mathbf{h}}_u + \tilde{\mathbf{h}}_u, \quad (51)$$

where $\hat{\mathbf{h}}_u$ and $\tilde{\mathbf{h}}_u$ are statistically independent. The received signal at user u is given by

$$\begin{aligned} y_u &= \mathbf{h}_u^H \mathbf{x} + n_u \\ &= \sum_{i=1}^K \sqrt{P_i} \hat{\mathbf{h}}_u^H \mathbf{w}_i x_i + \sum_{i=1}^K \sqrt{P_i} \tilde{\mathbf{h}}_u^H \mathbf{w}_i x_i + n_u. \end{aligned} \quad (52)$$

Since ZF precoding ensures that $\hat{\mathbf{h}}_u^H \mathbf{w}_i = 0$ for $i \neq u$, the received signal reduces to

$$\begin{aligned} y_u &= \sqrt{P_u} \hat{\mathbf{h}}_u^H \mathbf{w}_u x_u + \sqrt{P_u} \tilde{\mathbf{h}}_u^H \mathbf{w}_u x_u \\ &\quad + \sum_{i \neq u} \sqrt{P_i} \tilde{\mathbf{h}}_u^H \mathbf{w}_i x_i + n_u, \end{aligned} \quad (53)$$

where the first term represents the desired signal component formed along the estimated channel direction. The second term corresponds to residual self-interference due to estimation errors, while the third term represents multiuser interference caused by imperfect channel knowledge.

C. SINR Expression

Due to channel estimation errors, the BS performs ZF precoding based on $\hat{\mathbf{H}}$ instead of the true channel \mathbf{H} . Using the standard use-and-forget bound [62], we treat the unknown channel estimation errors as additional Gaussian noise and condition on the channel estimates. Accordingly, the effective SINR at user u can be expressed as

$$\gamma_u = \frac{P_u |\hat{\mathbf{h}}_u^H \mathbf{w}_u|^2}{\sum_{i=1}^K P_i \mathbb{E}\{|\tilde{\mathbf{h}}_u^H \mathbf{w}_i|^2 | \hat{\mathbf{H}}\} + \sigma^2}. \quad (54)$$

Given that $\tilde{\mathbf{h}}_u$ is independent of $\hat{\mathbf{H}}$, and \mathbf{w}_i is a deterministic function of $\hat{\mathbf{H}}$, the conditional interference term becomes

$$\mathbb{E}\{|\tilde{\mathbf{h}}_u^H \mathbf{w}_i|^2 | \hat{\mathbf{H}}\} = \mathbf{w}_i^H \mathbf{C}_{\tilde{h},u} \mathbf{w}_i, \quad (55)$$

in which $\mathbf{C}_{\tilde{h},u} = \mathbb{E}\{\tilde{\mathbf{h}}_u \tilde{\mathbf{h}}_u^H\}$. Under the fading assumption $\mathbf{C}_{\tilde{h},u} = \Omega_{\tilde{h},u} \mathbf{I}_M$ and since $\|\mathbf{w}_i\|^2 = 1$, we obtain

$$\mathbb{E}\{|\tilde{\mathbf{h}}_u^H \mathbf{w}_i|^2 | \hat{\mathbf{H}}\} = \Omega_{\tilde{h},u}. \quad (56)$$

Hence, the SINR becomes

$$\gamma_u = \frac{P_u |\hat{\mathbf{h}}_u^H \mathbf{w}_u|^2}{\Omega_{\tilde{h},u} \sum_{i=1}^K P_i + \sigma^2}. \quad (57)$$

It should be noted that in the E-FAS setting both the desired signal term and the interference components depend explicitly on the topology-dependent routing gain β , through the estimation variances $\Omega_{\hat{h}}$ and $\Omega_{\tilde{h}}$. This dependence fundamentally governs the high-SNR behavior, to be analyzed next.

D. Distribution of the Effective Channel Gain

Under the two-timescale channel model,

$$\hat{\mathbf{h}}_u = \sqrt{\beta_u} \hat{\mathbf{g}}_u, \quad (58)$$

and assuming uncorrelated Rayleigh fading $\mathbf{R}_u = \mathbf{I}_M$, the channel estimate satisfies

$$\hat{\mathbf{h}}_u \sim \mathcal{CN}(\mathbf{0}, \Omega_{\hat{h},u} \mathbf{I}_M). \quad (59)$$

Since the ZF precoder nulls the estimated channels of the other $K - 1$ users, the effective beamforming vector \mathbf{w}_u lies in an $(M - K + 1)$ -dimensional subspace orthogonal to $\{\hat{\mathbf{h}}_i\}_{i \neq u}$. Accordingly, the effective channel gain $|\hat{\mathbf{h}}_u^H \mathbf{w}_u|^2$ is Gamma distributed with shape parameter $M - K + 1$ and scale parameter $\Omega_{\hat{h},u}$ [64], [65], i.e.,

$$Z_u \triangleq |\hat{\mathbf{h}}_u^H \mathbf{w}_u|^2 \sim \Gamma(M - K + 1, \Omega_{\hat{h},u}). \quad (60)$$

Now, assuming equal power allocation $P_u = P/K$, the SINR simplifies to

$$\gamma_u = \frac{\frac{P}{K} Z_u}{P \Omega_{\hat{h},u} + \sigma^2}, \quad (61)$$

where $Z_u \sim \Gamma(M - K + 1, \Omega_{\hat{h},u})$.

E. Achievable Sum-Rate with Training Overhead

Accounting for pilot overhead within each coherence block of length T_c , the achievable ergodic sum-rate is given by

$$R_{\text{sum}} = \left(1 - \frac{\tau_p}{T_c}\right) \sum_{u=1}^K \mathbb{E}\{\log_2(1 + \gamma_u)\}. \quad (62)$$

Under statistical symmetry among users and equal power allocation $P_u = P/K$, all users experience identical SINR statistics. Hence, the sum-rate can be defined as

$$R_{\text{sum}} \triangleq \left(1 - \frac{\tau_p}{T_c}\right) K \mathbb{E}\left[\log_2\left(1 + \frac{\frac{P}{K} Z}{P \Omega_{\hat{h}} + \sigma^2}\right)\right], \quad (63)$$

where $Z \sim \Gamma(M - K + 1, \Omega_{\hat{h}})$.

Assuming $a \triangleq \frac{P/K}{P \Omega_{\hat{h}} + \sigma^2}$, the expectation can be written as

$$\begin{aligned} R_{\text{sum}} &= \left(1 - \frac{\tau_p}{T_c}\right) \frac{K}{\ln 2} \\ &\times \int_0^\infty \ln(1 + ax) \frac{x^{M-K}}{\Gamma(M - K + 1) \Omega_{\hat{h}}^{M-K+1}} \exp\left(-\frac{x}{\Omega_{\hat{h}}}\right) dx. \end{aligned} \quad (64)$$

Using standard integral identities for Gamma-distributed random variables, the closed-form expression is obtained as

$$R_{\text{sum}} = \left(1 - \frac{\tau_p}{T_c}\right) \frac{K}{\ln 2} \exp(z) \sum_{m=1}^{M-K+1} E_m(z), \quad (65)$$

where $z = \frac{K(P \Omega_{\hat{h}} + \sigma^2)}{P \Omega_{\hat{h}}}$. The proof follows from the same analytical steps as in the single-user case, with the Gamma shape parameter adjusted from M to $M - K + 1$ to account for the ZF-induced dimensionality reduction.

F. High-SNR Analysis

As $P \rightarrow \infty$, the noise term becomes negligible compared to the residual interference term induced by channel estimation errors. Consequently, the SINR converges almost surely to

$$\gamma_{u,\infty} = \lim_{P \rightarrow \infty} \frac{\frac{P}{K} Z_u}{P \Omega_{\hat{h},u} + \sigma^2} = \frac{Z_u}{K \Omega_{\hat{h},u}}. \quad (66)$$

The result in (66) reveals that, under imperfect CSI, the multiuser ZF system becomes interference-limited at high SNR. Increasing the transmit power no longer improves the SINR, since both the desired signal and the residual interference scale linearly with P . Consequently, the achievable ergodic sum-rate exhibits the well-known high-SNR saturation behavior under imperfect CSI, and converges to

$$R_{\text{sum},\infty} = \left(1 - \frac{\tau_p}{T_c}\right) K \mathbb{E}\left[\log_2\left(1 + \frac{Z}{K \Omega_{\hat{h}}}\right)\right]. \quad (67)$$

The saturation level depends explicitly on the routing gain β_u via both $\Omega_{\hat{h},u}$ and $\Omega_{\tilde{h},u}$. A larger β_u improves the effective channel strength and reduces the estimation error variance, increasing the interference-limited ceiling [65]. While a similar dependence on large-scale fading also appears in conventional systems, a key distinction in the E-FAS setting is that the routing gain is topology-dependent and can be influenced through SW configuration. Hence, the high-SNR rate ceiling becomes inherently coupled with routing design, highlighting a distinctive feature of E-FAS-assisted transmission.

VI. NUMERICAL RESULTS

In this section, we evaluate the performance of E-FAS-assisted downlink transmission under imperfect CSI and validate the analytical expressions derived in the previous sections. The numerical results aim to quantify the impact of SW-assisted propagation, channel estimation quality, and pilot overhead on outage probability and achievable rate.

Unless otherwise specified, the simulation parameters are set as follows. The BS is equipped with $M = 64$ antennas. For the multiuser case, the BS serves $K = 8$ single-antenna users. The channel coherence block length is $T_c = 200$ symbols and the noise variance is normalized to $\sigma^2 = 1$. Uplink training is performed using orthogonal pilots with per-symbol pilot SNR $\rho_p/\sigma^2 = 0$ dB, i.e., $\rho_p = 1$. The pilot length is set to $\tau_p = K$ in the multiuser case, as commonly adopted for orthogonal pilot transmission in TDD multiuser MIMO systems [61], while in the single-user case, $\tau_p = 8$ is adopted as a representative operating point that provides a reasonable trade-off between channel estimation accuracy and pilot overhead, unless stated otherwise. The downlink SNR is defined as $\rho_d \triangleq P/\sigma^2$ and is varied over $[-10, 30]$ dB. Furthermore, the equivalent end-to-end channel is modeled as $\mathbf{h}_u \sim \mathcal{CN}(\mathbf{0}, \beta \mathbf{I}_M)$, where β denotes the large-scale channel power capturing the end-to-end propagation gain. For simplicity and to isolate the impact of CSI quality, symmetric large-scale conditions are assumed for all users. Unless otherwise stated, we assume $\beta_u = \beta$ for all users. Additionally, to comprehensively evaluate the influence of CSI accuracy on system performance, we consider the following benchmark schemes:

- Ideal transmission assuming perfect CSI,

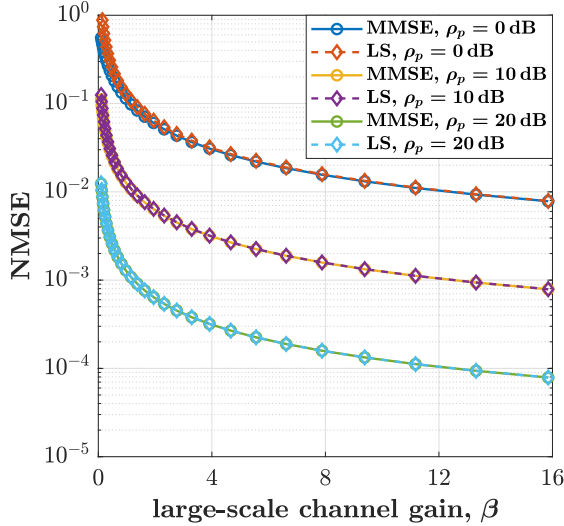


Fig. 2. NMSE versus routing gain β for LS and MMSE estimators under different pilot SNR values.

- Imperfect CSI based on MMSE channel estimation,
- Imperfect CSI based on LS channel estimation,
- Conventional transmission scheme without E-FAS.

Moreover, to ensure a physically meaningful comparison between the E-FAS-assisted and conventional transmission scenarios, we consider a representative large-scale propagation geometry. Specifically, a direct BS-user link of distance d_0 is assumed for the conventional case, whereas the E-FAS-assisted route consists of two segments with distances d_1 (BS-E-FAS) and d_2 (E-FAS-user). The large-scale channel gain is modeled using a standard distance-dependent path-loss model $\beta(d) = C_0 \left(\frac{d}{d_0}\right)^{-\alpha}$, where α denotes the path-loss exponent and C_0 is chosen such that the direct link satisfies $\beta_{\text{no}} = 1$ at distance d_0 . The composite gain of the E-FAS-assisted path therefore depends on the relative segment distances and α , and can yield a moderate large-scale enhancement (on the order of a few dB) under representative configurations. In the subsequent analysis, β is treated parametrically for analytical tractability, while the above geometry provides a physically grounded interpretation of the adopted gain values.

Fig. 2 depicts the normalized mean square error (NMSE) of LS and MMSE channel estimators versus the large-scale channel gain β under different pilot SNR levels $\rho_p \in \{0, 10, 20\}$ dB. As observed, the NMSE decreases monotonically with β . This behavior is expected since a larger β increases the effective pilot observation power, thereby improving the SNR ratio of the training phase and reducing the estimation error. Increasing the pilot SNR ρ_p further improves the NMSE across the entire β range, as higher pilot power mitigates the impact of additive noise during channel estimation. Moreover, the MMSE estimator provides noticeable performance gains over LS in the low- β and low- ρ_p regimes, where the pilot observations are noise-limited. This improvement stems from the exploitation of prior second-order channel statistics in MMSE estimation, whereas LS relies solely on the received pilot signal. As either β or ρ_p increases, the pilot observation quality

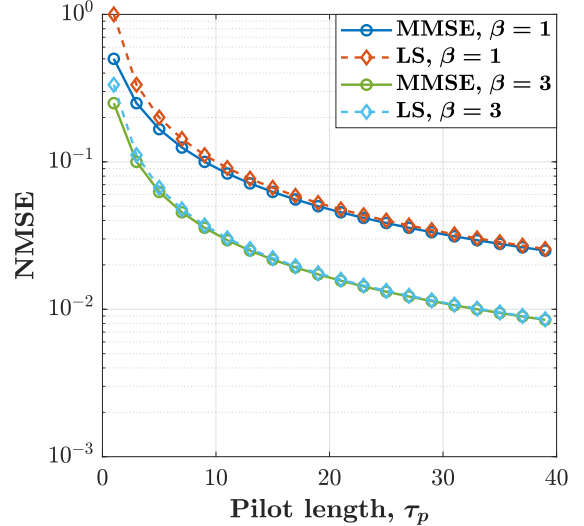


Fig. 3. NMSE versus pilot length τ_p at $\rho_p = 0$ dB for different β .

improves and the performance gap between MMSE and LS progressively diminishes. In high effective pilot SNR regimes, both estimators approach similar performance, reducing the relative benefit of statistical regularization.

Fig. 3 illustrates the NMSE as a function of the pilot length τ_p at $\rho_p = 0$ dB for $\beta \in \{1, 3\}$ under LS and MMSE estimation. The NMSE decreases monotonically with τ_p in all cases, as a longer pilot sequence increases the accumulated training energy $\tau_p \rho_p$ and therefore improves the effective observation SNR. For a fixed estimator, the case with $\beta = 3$ yields lower NMSE compared to $\beta = 1$, reflecting the fact that a stronger large-scale channel gain enhances the received pilot signal power and improves channel reconstruction reliability. Moreover, the MMSE estimator provides lower NMSE than LS for both values of β , with the most pronounced difference observed at small τ_p . In this regime, the limited training energy renders the estimation noise-limited, and the statistical regularization inherent in MMSE offers additional robustness. As τ_p increases, the performance gap progressively diminishes, since the improved observation quality reduces the relative impact of prior statistical information.

In Fig. 4, we present the outage probability as a function of the downlink SNR ρ_d . The close agreement between the Monte Carlo simulations and the analytical curves confirms the correctness of the derived outage expressions. It is observed that the outage probability decreases monotonically with ρ_d for all schemes, since increasing the transmit SNR enhances the received signal power and improves the likelihood that the instantaneous SINR exceeds the target threshold. A clear performance gap is observed between the E-FAS-assisted and conventional (No E-FAS) transmission. For a given outage level, the E-FAS scheme requires substantially lower ρ_d , which reflects the large-scale gain β introduced by SW-assisted propagation. This gain effectively shifts the SINR distribution toward higher values, yielding a noticeable SNR advantage. As expected, perfect CSI provides an upper performance bound in both propagation scenarios. Channel estimation errors reduce

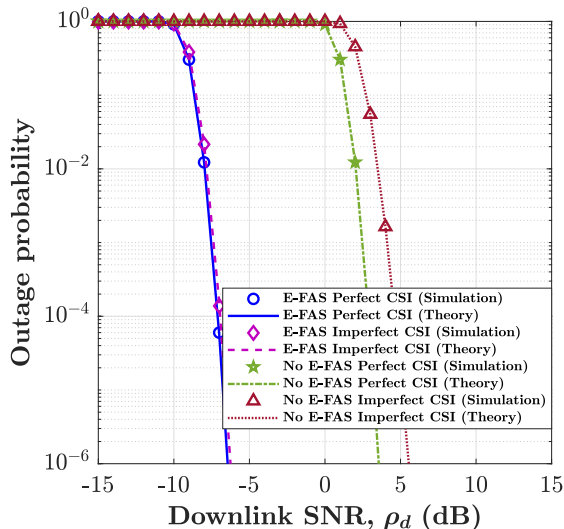


Fig. 4. Outage probability versus downlink SNR ρ_d for $M = 64$, $\tau_p = 8$, and $\rho_p = 0$ dB.

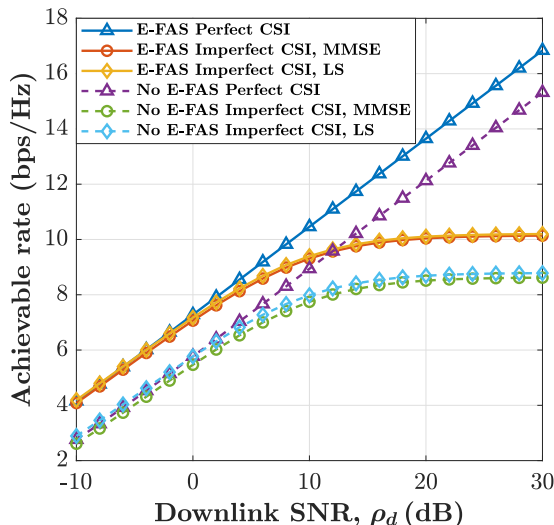


Fig. 5. Achievable single-user rate versus downlink SNR ρ_d under MRT precoding with training overhead.

the effective beamforming gain and introduce additional self-interference components arising from the mismatch between the true and estimated channels, resulting in a rightward shift of the outage curves. Under the considered parameter configuration, however, the performance gap between perfect and imperfect CSI remains moderate, particularly in the E-FAS case. This behavior is mainly due to the relatively high effective pilot SNR and the substantial array gain provided by $M = 64$ antennas, which together enable accurate channel reconstruction and robust MRT beamforming.

Fig. 5 shows the single-user rate versus the downlink SNR ρ_d , accounting for pilot overhead with $M = 64$, $\tau_p = 8$, and $T_c = 200$. First, we observe that the perfect CSI curves increase almost linearly with ρ_d (in dB scale), reflecting the continuous growth of the effective received SNR due to coherent beamforming and array gain. In contrast, the imperfect CSI

curves exhibit a clear saturation at high SNR. This behavior follows directly from the SINR expression under imperfect CSI, where the residual self-interference term $P\Omega_{\tilde{h}_i}$ scales linearly with the transmit power P . As ρ_d increases, both the desired signal and the estimation-error-induced interference grow proportionally, leading to a finite SINR ceiling and thus a rate saturation. The E-FAS-assisted transmission consistently outperforms the conventional case across the entire SNR range. This gain originates from the larger large-scale channel coefficient β , which enhances both the beamforming gain and the quality of channel estimation. Moreover, the MMSE estimator achieves higher rates than the LS estimator, particularly in the moderate-to-high SNR regime. The improved performance stems from the reduced estimation error variance under MMSE, which directly increases the SINR ceiling. At low SNR, the performance gap between MMSE and LS becomes smaller, since the system operates in a noise-limited regime where the impact of CSI errors is less dominant.

Fig. 6 depicts the single-user rate versus the pilot length τ_p at $\rho_d = 10$ dB. Under imperfect CSI, the rate exhibits a clear unimodal behavior. When τ_p is small, the channel estimation quality is poor due to insufficient training energy, resulting in a large estimation error variance and a reduced effective SINR. As τ_p increases, the improved channel estimation enhances the beamforming gain and increases the achievable rate. However, beyond a certain point, further increasing τ_p reduces the fraction of symbols available for data transmission through the pre-log penalty, causing the achievable rate to decrease. While this trade-off is inherent to pilot-based transmission, in the E-FAS architecture, the routing gain β directly affects the effective pilot SNR and thus shifts the optimal training length. In contrast, under perfect CSI, no estimation error is present and increasing τ_p only reduces the available data transmission time. Consequently, the rate decreases monotonically with τ_p in the perfect CSI case. Furthermore, the E-FAS-assisted transmission consistently achieves higher rates than the conventional scenario due to the larger large-scale channel gain β , which enhances the effective received SNR. The MMSE estimator slightly outperforms the LS estimator across the considered range, as it yields a smaller estimation error variance and thus a higher effective SINR.

Fig. 7 presents the multiuser ZF ergodic sum-rate versus the downlink SNR ρ_d with pilot overhead, where $M = 64$ and $K = 8$. Under perfect CSI, the sum-rate increases almost linearly with ρ_d (in dB scale), reflecting the full spatial multiplexing gain achieved by ZF precoding when inter-user interference is perfectly suppressed. The E-FAS-assisted system achieves a consistently higher sum-rate than the conventional transmission due to the enhanced large-scale channel gain, which effectively increases the received SNR for all users. In contrast, under imperfect CSI, the sum-rate exhibits a clear saturation behavior at high SNR. This phenomenon arises from residual multiuser interference caused by channel estimation errors. As the transmit power increases, both the desired signal and the interference terms scale proportionally with P , while the estimation error variance remains non-zero. Consequently, the SINR converges to a finite limit, and the system becomes interference-limited rather than noise-limited.

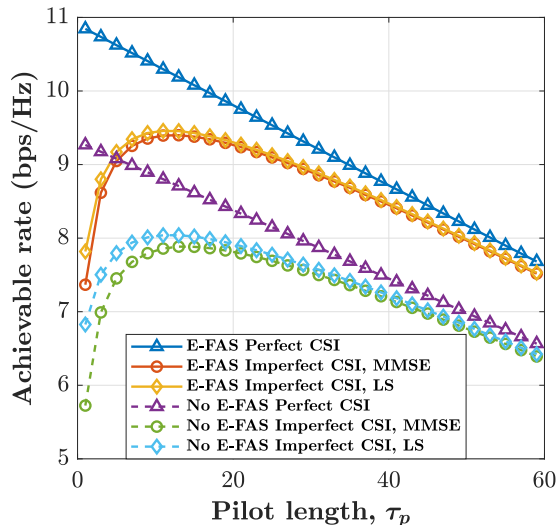


Fig. 6. Achievable single-user rate versus pilot length τ_p at fixed SNR.

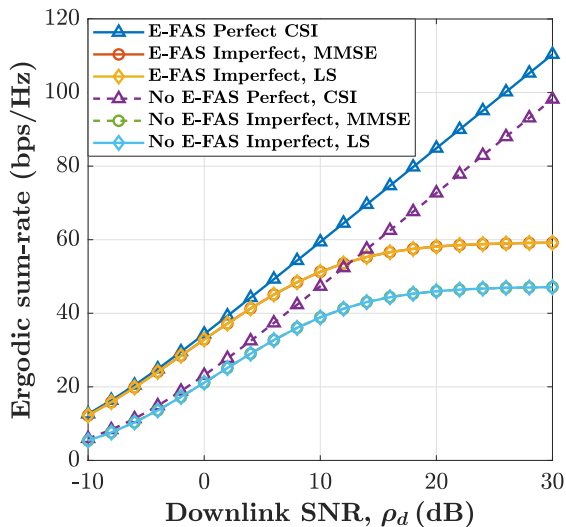


Fig. 7. Ergodic sum-rate versus downlink SNR ρ_d for multiuser ZF transmission with training overhead.

It is further observed that the performance gap between MMSE and LS estimators is relatively small in this multiuser setting. This behavior is mainly because at moderate-to-high SNR, the dominant performance degradation stems from residual interference due to imperfect CSI, rather than from the specific structure of the estimator. Finally, the E-FAS-assisted transmission retains a noticeable advantage over the non-E-FAS case even under imperfect CSI, demonstrating that the large-scale routing gain not only enhances the desired signal power but also improves the robustness of spatial multiplexing.

Fig. 8 illustrates the multiuser ZF ergodic sum-rate versus the number of served users K at $\rho_d = 10$ dB, with $M = 64$ and orthogonal pilot allocation $\tau_p = K$. We see that the sum-rate increases with K over the shown range. This trend reflects the spatial multiplexing gain of the system: serving more users allows the BS to exploit additional spatial DoF, thereby increasing the total throughput. Since $M = 64$ is

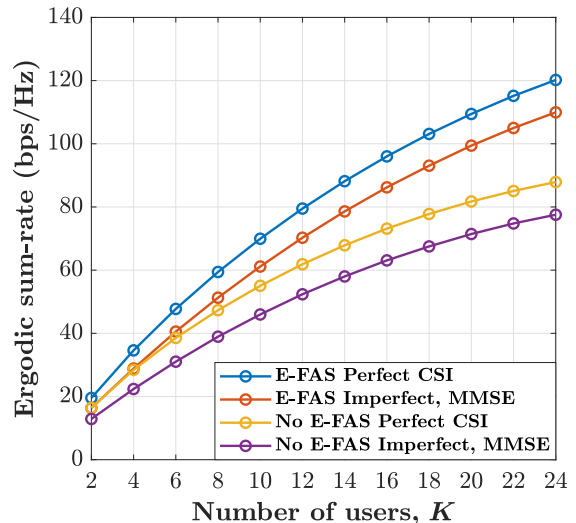


Fig. 8. Ergodic sum-rate versus number of users K for ZF precoding at fixed SNR.

significantly larger than the values of K , the ZF precoder can effectively separate users, and the multiplexing gain dominates. However, increasing K also increases the pilot overhead due to the orthogonal pilot requirement $\tau_p = K$, which reduces the effective pre-log factor $(1 - \tau_p/T_c)$. Consequently, although the sum-rate grows with K in the considered range, the growth rate gradually decreases, indicating the emerging impact of training overhead. For sufficiently large K , the pre-log penalty would eventually dominate and limit further gains. It is further observed that the E-FAS-assisted transmission consistently achieves higher sum-rate than the conventional scenario without E-FAS. This gain stems from the enhanced large-scale channel gain, which improves the effective SINR of all users and strengthens the spatial multiplexing performance. Additionally, it is observed that the imperfect CSI introduces a noticeable performance degradation compared to perfect CSI due to residual multiuser interference. Nevertheless, the performance gap remains bounded, indicating that the proposed system retains substantial multiplexing benefits even under practical channel estimation constraints.

VII. CONCLUSION

This paper investigated the impact of imperfect CSI on E-FAS-assisted downlink transmission. We considered a practical pilot-based estimation framework and developed a tractable MMSE channel estimation model for the equivalent E-FAS channel. Closed-form expressions were derived for the statistics of the estimated channel and the associated estimation error. For the single-user case, analytical expressions for outage probability and ergodic rate were obtained under imperfect CSI, revealing a fundamental high-SNR performance saturation caused by residual estimation errors. For the multiuser case, ZF precoding based on imperfect CSI estimates was studied, and the resulting residual-interference-limited SINR and ergodic sum-rate behavior were characterized. Our analysis demonstrated that CSI estimation errors impose an intrinsic performance ceiling in the high-SNR regime. Despite these

limitations, our results showed that E-FAS preserves its large-scale power-gain advantages over conventional space wave transmission even under imperfect CSI.

APPENDIX A

CLOSED-FORM EVALUATION OF THE ACHIEVABLE RATE

Consider the integral in (44) as

$$I \triangleq \int_0^\infty \ln\left(1 + \frac{Px}{P\Omega_{\tilde{h}} + \sigma^2}\right) \frac{x^{M-1}}{\Gamma(M)\Omega_{\tilde{h}}^M} \exp\left(-\frac{x}{\Omega_{\tilde{h}}}\right) dx, \quad (68)$$

where $M \in \{1, 2, \dots\}$, $\Omega_{\tilde{h}} > 0$, and $P\Omega_{\tilde{h}} + \sigma^2 > 0$. By defining the positive constants as

$$a \triangleq \frac{P}{P\Omega_{\tilde{h}} + \sigma^2} \quad \text{and} \quad z \triangleq \frac{1}{a\Omega_{\tilde{h}}} = \frac{P\Omega_{\tilde{h}} + \sigma^2}{P\Omega_{\tilde{h}}}, \quad (69)$$

and the change of variables $x = \Omega_{\tilde{h}}t$, (68) becomes

$$I = \frac{1}{\Gamma(M)} \int_0^\infty \ln\left(1 + \frac{t}{z}\right) t^{M-1} e^{-t} dt. \quad (70)$$

Now, let

$$F_M(z) \triangleq \frac{1}{\Gamma(M)} \int_0^\infty \ln\left(1 + \frac{t}{z}\right) t^{M-1} e^{-t} dt. \quad (71)$$

By differentiating (71) under the integral sign, we have

$$\begin{aligned} \frac{dF_M(z)}{dz} &= \frac{1}{\Gamma(M)} \int_0^\infty \frac{\partial}{\partial z} \ln\left(1 + \frac{t}{z}\right) t^{M-1} e^{-t} dt \\ &= -\frac{1}{\Gamma(M)} \int_0^\infty \frac{t}{z(z+t)} t^{M-1} e^{-t} dt \\ &= -\frac{1}{z\Gamma(M)} \int_0^\infty \frac{t^M}{z+t} e^{-t} dt. \end{aligned} \quad (72)$$

Using the identity $\frac{1}{z+t} = \int_0^\infty e^{-(z+t)u} du$ for $z > 0$, (72) becomes

$$\begin{aligned} \frac{dF_M(z)}{dz} &= -\frac{1}{z\Gamma(M)} \int_0^\infty \left(\int_0^\infty t^M e^{-t} e^{-(z+t)u} dt \right) du \\ &= -\frac{1}{z\Gamma(M)} \int_0^\infty e^{-zu} \left(\int_0^\infty t^M e^{-(1+u)t} dt \right) du. \end{aligned} \quad (73)$$

Since $\int_0^\infty t^M e^{-(1+u)t} dt = \Gamma(M+1)(1+u)^{-(M+1)}$, (73) yields

$$\begin{aligned} \frac{dF_M(z)}{dz} &= -\frac{\Gamma(M+1)}{z\Gamma(M)} \int_0^\infty \frac{e^{-zu}}{(1+u)^{M+1}} du \\ &= -\frac{M}{z} \int_0^\infty \frac{e^{-zu}}{(1+u)^{M+1}} du. \end{aligned} \quad (74)$$

With the substitution $s = 1 + u$, we obtain

$$\frac{dF_M(z)}{dz} = -\frac{M}{z} e^{-z} \int_1^\infty \frac{e^{-zs}}{s^{M+1}} ds = -\frac{M}{z} e^{-z} E_{M+1}(z), \quad (75)$$

where the generalized exponential integral is defined as

$$E_n(z) \triangleq \int_1^\infty \frac{e^{-zt}}{t^n} dt, \quad z > 0, \quad n \geq 1. \quad (76)$$

Using the standard recurrence

$$nE_{n+1}(z) = e^{-z} - zE_n(z), \quad n \geq 1, \quad (77)$$

(75) simplifies to

$$\frac{dF_M(z)}{dz} = -\frac{1}{z} + e^{-z} E_M(z). \quad (78)$$

Now, we define

$$G_M(z) \triangleq e^{-z} \sum_{k=1}^M E_k(z). \quad (79)$$

Using the derivative identity $\frac{d}{dz} E_k(z) = -E_{k-1}(z)$ for $k \geq 2$ and $\frac{d}{dz} E_1(z) = -e^{-z}/z$, it follows that

$$\frac{dG_M(z)}{dz} = -\frac{1}{z} + e^{-z} E_M(z), \quad (80)$$

which matches (78). Therefore, $F_M(z) = G_M(z) + C$ for some constant C . Since $F_M(z) \rightarrow 0$ as $z \rightarrow \infty$ (equivalently $a \rightarrow 0$), and $e^{-z} E_k(z) \rightarrow 0$ as $z \rightarrow \infty$, we have $C = 0$. Hence,

$$I = F_M(z) = e^{-z} \sum_{k=1}^M E_k(z), \quad z = \frac{P\Omega_{\tilde{h}} + \sigma^2}{P\Omega_{\tilde{h}}}. \quad (81)$$

REFERENCES

- [1] M. Matthaiou *et al.*, "The road to 6G: Ten physical layer challenges for communications engineers," *IEEE Commun. Mag.*, vol. 59, no. 1, pp. 64–69, Jan. 2021.
- [2] F. Tariq *et al.*, "A speculative study on 6G," *IEEE Wireless Commun.*, vol. 27, no. 4, pp. 118–125, Aug. 2020.
- [3] W. Jiang, B. Han, M. A. Habibi and H. D. Schotten, "The road towards 6G: A comprehensive survey," *IEEE Open J. Commun. Soc.*, vol. 2, pp. 334–366, Feb. 2021.
- [4] T. S. Rappaport *et al.*, "Overview of millimeter wave communications for fifth-generation (5G) wireless networks—with a focus on propagation models," *IEEE Trans. Antennas Propag.*, vol. 65, no. 12, pp. 6213–6230, Dec. 2017.
- [5] S. Rangan, T. S. Rappaport and E. Erkip, "Millimeter-wave cellular wireless networks: Potentials and challenges," *Proc. IEEE*, vol. 102, no. 3, pp. 366–385, Mar. 2014.
- [6] R. W. Heath, N. González-Prelcic, S. Rangan, W. Roh and A. M. Sayeed, "An overview of signal processing techniques for millimeter wave MIMO systems," *IEEE J. Select. Topics Sig. Proc.*, vol. 10, no. 3, pp. 436–453, Apr. 2016.
- [7] E. Basar *et al.*, "Wireless communications through reconfigurable intelligent surfaces," *IEEE Access*, vol. 7, pp. 116753–116773, 2019.
- [8] C. Huang, A. Zappone, G. C. Alexandropoulos, M. Debbah, and C. Yuen, "Reconfigurable intelligent surfaces for energy efficiency in wireless communication," *IEEE Trans. Wireless Commun.*, vol. 18, no. 8, pp. 4157–4170, Aug. 2019.
- [9] E. Björnson, Ö. Özdogan and E. G. Larsson, "Intelligent reflecting surface versus decode-and-forward: How large surfaces are needed to beat relaying?," *IEEE Wireless Commun. Lett.*, vol. 9, no. 2, pp. 244–248, Feb. 2020.
- [10] K. K. Wong, A. Shojaeifard, K.-F. Tong and Y. Zhang, "Fluid antenna systems," *IEEE Trans. Wireless Commun.*, vol. 20, no. 3, pp. 1950–1962, Mar. 2021.
- [11] K. K. Wong, A. Shojaeifard, K.-F. Tong and Y. Zhang, "Performance limits of fluid antenna systems," *IEEE Commun. Lett.*, vol. 24, no. 11, pp. 2469–2472, Nov. 2020.
- [12] W. K. New *et al.*, "A tutorial on fluid antenna system for 6G networks: Encompassing communication theory, optimization methods and hardware designs," *IEEE Commun. Surv. Tuts.*, vol. 27, no. 4, pp. 2325–2377, Aug. 2025.
- [13] W.-J. Lu *et al.*, "Fluid antennas: Reshaping intrinsic properties for flexible radiation characteristics in intelligent wireless networks," *IEEE Commun. Mag.*, vol. 63, no. 5, pp. 40–45, May 2025.
- [14] H. Hong *et al.*, "A contemporary survey on fluid antenna systems: Fundamentals and networking perspectives," *IEEE Trans. Netw. Sci. Eng.*, vol. 13, pp. 2305–2328, 2026.
- [15] W. K. New *et al.*, "Fluid antenna systems: Redefining reconfigurable wireless communications," *IEEE J. Sel. Areas Commun.*, vol. 44, pp. 1013–1044, 2026.

- [16] T. Wu *et al.*, “Fluid antenna systems enabling 6G: Principles, applications, and research directions,” to appear in *IEEE Wireless Commun.*, DOI:10.1109/MWC.2025.3629597, 2025.
- [17] Y. Shen *et al.*, “Design and experimental validation of mmWave surface wave enabled fluid antennas for future wireless communications,” to appear in *IEEE Antennas & Wireless Propag. Lett.*, DOI:10.1109/LAWP.2026.3657059, 2026.
- [18] R. Wang *et al.*, “Electromagnetically reconfigurable fluid antenna system for wireless communications: Design, modeling, algorithm, fabrication, and experiment,” *IEEE J. Select. Areas Commun.*, vol. 44, pp. 1464–1479, 2026.
- [19] J. Zhang *et al.*, “A novel pixel-based reconfigurable antenna applied in fluid antenna systems with high switching speed,” *IEEE Open J. Antennas & Propag.*, vol. 6, no. 1, pp. 212–228, Feb. 2025.
- [20] B. Liu, T. Wu, K. K. Wong, H. Wong, and K. F. Tong, “Wideband pixel-based fluid antenna system: An antenna design for smart city,” *IEEE Internet Things J.*, vol. 13, no. 4, pp. 6850–6862, Feb. 2026.
- [21] K. K. Wong, C. Wang, S. Shen, C.-B. Chae and R. Murch, “Reconfigurable pixel antennas meet fluid antenna systems: A paradigm shift to electromagnetic signal and information processing,” *IEEE Wireless Commun.*, vol. 33, no. 1, pp. 191–198, Feb. 2026.
- [22] S. Zhang *et al.*, “Fluid antenna systems enabled by reconfigurable holographic surfaces: Beamforming design and experimental validation,” *IEEE J. Select. Areas Commun.*, vol. 44, pp. 1417–1431, 2026.
- [23] B. Liu, K.-F. Tong, K. K. Wong, C.-B. Chae, and H. Wong, “Programmable meta-fluid antenna for spatial multiplexing in fast fluctuating radio channels,” *Optics Express*, vol. 33, no. 13, pp. 28898–28915, 2025.
- [24] K. F. Tong, B. Liu, and K. K. Wong. “Designs and challenges in fluid antenna system hardware.” *Electronics*, vol. 14, no. 7, pp. 1458, 2025.
- [25] M. Khammassi, A. Kammoun, and M.-S. Alouini, “A new analytical approximation of the fluid antenna system channel,” *IEEE Trans. Wireless Commun.*, vol. 22, no. 12, pp. 8843–8858, Dec. 2023.
- [26] W. K. New, K. K. Wong, H. Xu, K.-F. Tong and C.-B. Chae, “Fluid antenna system: New insights on outage probability and diversity gain,” *IEEE Trans. Wireless Commun.*, vol. 23, no. 1, pp. 128–140, Jan. 2024.
- [27] W. K. New, K. K. Wong, H. Xu, K.-F. Tong and C.-B. Chae, “An information-theoretic characterization of MIMO-FAS: Optimization, diversity-multiplexing tradeoff and q -outage capacity,” *IEEE Trans. Wireless Commun.*, vol. 23, no. 6, pp. 5541–5556, Jun. 2024.
- [28] F. Rostami Ghadi *et al.*, “A Gaussian copula approach to the performance analysis of fluid antenna systems,” *IEEE Trans. Wireless Commun.*, vol. 23, no. 11, pp. 17573–17585, Nov. 2024.
- [29] P. Ramírez-Espinosa, D. Morales-Jimenez and K. K. Wong, “A new spatial block-correlation model for fluid antenna systems,” *IEEE Trans. Wireless Commun.*, vol. 23, no. 11, pp. 15829–15843, Nov. 2024.
- [30] J. D. Vega-Sánchez, L. Urquiza-Aguiar, M. C. P. Paredes and D. P. M. Osorio, “A simple method for the performance analysis of fluid antenna systems under correlated Nakagami- m fading,” *IEEE Wireless Commun. Lett.*, vol. 13, no. 2, pp. 377–381, Feb. 2024.
- [31] Y. Chen and T. Xu, “Fluid antenna index modulation communications,” *IEEE Wireless Commun. Lett.*, vol. 13, no. 4, pp. 1203–1207, Apr. 2024.
- [32] J. Zhu *et al.*, “Index modulation for fluid antenna-assisted MIMO communications: System design and performance analysis,” *IEEE Trans. Wireless Commun.*, vol. 23, no. 8, pp. 9701–9713, Aug. 2024.
- [33] H. Yang *et al.*, “Position index modulation for fluid antenna system,” *IEEE Trans. Wireless Commun.*, vol. 23, no. 11, pp. 16773–16787, Nov. 2024.
- [34] X. Guo *et al.*, “Fluid antenna index modulation for MIMO systems: Robust transmission and low-complexity detection,” *IEEE Trans. Commun.*, vol. 73, no. 12, pp. 15955–15970, Dec. 2025.
- [35] W. K. New *et al.*, “Fluid antenna system enhancing orthogonal and non-orthogonal multiple access,” *IEEE Commun. Lett.*, vol. 28, no. 1, pp. 218–222, Jan. 2024.
- [36] F. R. Ghadi, K. K. Wong, F. J. López-Martínez, L. Hanzo, and C.-B. Chae, “Fluid antenna-aided rate-splitting multiple access,” *IEEE Trans. Veh. Technol.*, vol. 75, no. 2, pp. 3417–3422, Feb. 2026.
- [37] F. R. Ghadi *et al.*, “Phase-mismatched STAR-RIS with FAS-assisted RSMA users,” *IEEE Trans. Commun.*, vol. 74, pp. 2032–2046, 2026.
- [38] C. Wang *et al.*, “Fluid antenna system liberating multiuser MIMO for ISAC via deep reinforcement learning,” *IEEE Trans. Wireless Commun.*, vol. 23, no. 9, pp. 10879–10894, Sept. 2024.
- [39] J. Zou *et al.*, “Shifting the ISAC trade-off with fluid antenna systems,” *IEEE Wireless Commun. Lett.*, vol. 13, no. 12, pp. 3479–3483, Dec. 2024.
- [40] L. Zhou, J. Yao, M. Jin, T. Wu and K. K. Wong, “Fluid antenna-assisted ISAC systems,” *IEEE Wireless Commun. Lett.*, vol. 13, no. 12, pp. 3533–3537, Dec. 2024.
- [41] F. Rostami Ghadi, K. K. Wong, F. Javier López-Martínez, H. Shin and L. Hanzo, “Performance analysis of FAS-aided NOMA-ISAC: A backscattering scenario,” *IEEE Internet Things J.*, vol. 12, no. 23, pp. 51326–51340, Dec., 2025.
- [42] B. Tang *et al.*, “Full-duplex FAS-assisted base station for ISAC,” *IEEE Trans. Wireless Commun.*, vol. 25, pp. 2922–2938, 2025.
- [43] B. Tang *et al.*, “Fluid antenna enabling secret communications,” *IEEE Commun. Lett.*, vol. 27, no. 6, pp. 1491–1495, Jun. 2023.
- [44] J. D. Vega-Sánchez, L. F. Urquiza-Aguiar, H. R. C. Mora, N. V. O. Garzón and D. P. M. Osorio, “Fluid antenna system: Secrecy outage probability analysis,” *IEEE Trans. Veh. Technol.*, vol. 73, no. 8, pp. 11458–11469, Aug. 2024.
- [45] F. Rostami Ghadi *et al.*, “Physical layer security over fluid antenna systems: Secrecy performance analysis,” *IEEE Trans. Wireless Commun.*, vol. 23, no. 12, pp. 18201–18213, Dec. 2024.
- [46] J. Yao *et al.*, “FAS for secure and covert communications,” *IEEE Internet Things J.*, vol. 12, no. 11, pp. 18414–18418, Jun. 2025.
- [47] F. Rostami Ghadi *et al.*, “On performance of RIS-aided fluid antenna systems,” *IEEE Wireless Commun. Lett.*, vol. 13, no. 8, pp. 2175–2179, Aug. 2024.
- [48] X. Zhang *et al.*, “Fluid antenna meets RIS: Random matrix analysis and two-timescale design for multi-user communications,” *IEEE J. Select. Areas Commun.*, DOI:10.1109/JSAC.2025.3615911, 2025.
- [49] J. Yao *et al.*, “FAS-RIS communication: Model, analysis, and optimization,” *IEEE Trans. Veh. Technol.*, vol. 74, no. 6, pp. 9938–9943, Jun. 2025.
- [50] J. Zheng *et al.*, “Unlocking FAS-RIS security analysis with block-correlation model,” *IEEE Wireless Commun. Lett.*, vol. 14, no. 7, pp. 2029–2033, Jul. 2025.
- [51] A. Salem, K. K. Wong, G. Alexandropoulos, C.-B. Chae, and R. Murch, “A first look at the performance enhancement potential of fluid reconfigurable intelligent surface,” *arXiv preprint*, arXiv:2502.17116, 2025.
- [52] H. Xiao *et al.*, “Fluid reconfigurable intelligent surfaces: Joint on-off selection and beamforming with discrete phase shifts,” *IEEE Wireless Commun. Lett.*, vol. 14, no. 10, pp. 3124–3128, Oct. 2025.
- [53] F. R. Ghadi *et al.*, “Performance analysis of wireless communication systems assisted by fluid reconfigurable intelligent surfaces,” *IEEE Wireless Commun. Lett.*, vol. 14, no. 12, pp. 3922–3926, Dec. 2025.
- [54] H. Xiao *et al.*, “Fluid reconfigurable intelligent surface with element-level pattern reconfigurability: Beamforming and pattern co-design,” *IEEE Trans. Wireless Commun.*, vol. 25, pp. 10791–10806, 2026.
- [55] F. Rostami Ghadi *et al.*, “Performance analysis of fluid reconfigurable intelligent surface over covert communications,” in *Proc. Int. Conf. 6G Netw. (6GNet)*, pp. 82–86, 17–19 Dec. 2025, Paris, France.
- [56] F. R. Ghadi *et al.*, “FIRES: Fluid integrated reflecting and emitting surfaces,” *IEEE Wireless Commun. Lett.*, vol. 14, no. 11, pp. 3744–3748, Nov. 2025.
- [57] F. Rostami Ghadi *et al.*, “Coverage analysis and optimization of FIRES-assisted NOMA and OMA systems,” *arXiv preprint*, arXiv:2511.01111, 2025.
- [58] K. K. Wong, K. F. Tong, Z. Chu, and Y. Zhang, “A vision to smart radio environment: Surface wave communication superhighways,” *IEEE Wireless Commun.*, vol. 28, no. 1, pp. 112–119, Feb. 2021.
- [59] K. K. Wong *et al.*, “Enormous fluid antenna systems (E-FAS): Rethinking the future of wireless communications,” *Research Square preprint*, <https://doi.org/10.21203/rs.3.rs-8002084/v1>, 2025.
- [60] F. Rostami Ghadi *et al.*, “Enormous fluid antenna systems (E-FAS) for multiuser MIMO: Channel modeling and analysis,” *arXiv preprint*, arXiv:2602.11099, 2026.
- [61] H. Q. Ngo, E. G. Larsson and T. L. Marzetta, “Energy and spectral efficiency of very large multiuser MIMO systems,” *IEEE Trans. Commun.*, vol. 61, no. 4, pp. 1436–1449, Apr. 2013.
- [62] E. Björnson, J. Hoydis and L. Sanguinetti, “Massive MIMO networks: Spectral, energy, and hardware efficiency,” *Foundations & Trends Sig. Proc.*, vol. 11, no. 3–4, pp. 154–655, 2017.
- [63] M. Medard, “The effect upon channel capacity in wireless communications of perfect and imperfect knowledge of the channel,” *IEEE Trans. Inf. Theory*, vol. 46, no. 3, pp. 933–946, May 2000.
- [64] A. M. Tulino and S. Verdú, *Random matrix theory and wireless communications*, Now Publishers Inc, 2004.
- [65] S. Wagner, R. Couillet, M. Debbah and D. T. M. Slock, “Large system analysis of linear precoding in correlated MISO broadcast channels under limited feedback,” *IEEE Trans. Inf. Theory*, vol. 58, no. 7, pp. 4509–4537, Jul. 2012.